Rationally Programmable Paper-Based Artificial Trees Toward Multipath Solar-Driven Water Extraction from Liquid/Solid Substrates

Peng Xiao, Jiang He, Yun Liang, Chang Zhang, Jincui Gu, Jiawei Zhang, Youju Huang, Shiao-Wei Kuo, and Tao Chen*

Solar vaporization, which is emerged as a promising candidate for harvesting solar energy in sewage purification and/or seawater desalination, has attracted increasing interests during the last few years. Although tremendous advances are made, it is still challenging to realize simple fabrication protocols, low-cost, and rationally editable 3D structures toward multipath water extraction from liquid/solid media. Inspired by natural plants with hierarchical structures rooted in soils, herein, an artificial tree of carbon nanotubes (CNTs) film/paper hybrid with tunable transpiration toward multipath water extraction under solar illumination is rationally designed. In this system, an interfacial-assisted transfer strategy is developed to alternatively transfer the self-assembled CNT films at the air/water interface onto one side of arbitrary substrates in a uniform/patterned way. The paper-based photothermal absorbers with favorable tailorability and foldability allow the transformation of the 2D evaporators to tree-like 3D ones. The achieved 3D evaporators with specific structures can extract purified water ranging from conventional liquid phase (e.g., water) to solid phase (e.g., sand), which can significantly extend the application of water extraction.

1. Introduction

Water vaporization that dominates the water cycle is ubiquitous in nature, in which the solar-to-thermal technologies can significantly boost the evaporation process.[1–3] Considering the growing problem of water shortage, harvesting solar energy for water distillation has aroused tremendous consideration due to its renewable and sustainable features.[4,5] Over the past few years, extensive efforts have been dedicated to develop sunlight absorber materials, such as plasmonic nanoparticles,[6–11] functional polymers,[12–14] carbon nanomaterials (exfoliated graphite,[15] graphene,[16–23] and carbon nanotubes [CNTs]),[24–27] Mxene sheets,[28,29] bilayer woods,[30,31] natural plants,[32,33] hierarchically nanostructured gels,[34,35] etc. However, there are still tremendous challenges, including expenses, scalability, foldability, and portability, which would severely restrict their potentials for practical applications.[36] Nowadays, most of these studies focused on the 2D interfacial vaporization platform, which suffered from the issues of low tridimensional utilization efficiency. In a confined system, building the 2D light-absorber units to a 3D framework is considered to be a direct and effective way to enhance the capability of purified water collection. More importantly, an adaptable capability to diverse environments is a vital factor that can extract water from liquid or solid substrates.

Plants that occupy most of the biosphere play critical roles in the ecosystem by sustaining the necessary oxygen food and energy for human survival. To harvest sufficient sunlight for indispensable photosynthesis, they enable themselves to grow in the 3D direction with hierarchical leaves and roots. The structural and environmental adaptation is a reliable and effective way to survive and reproduce over a long period of evolutionary process from sea to land.[37] Drawn inspiration from the natural plants, in which the roots, stems, and leaves perform water pumping, water transportation, and transpiration, respectively (**Figure 1**a), a concept of the bionic 3D architecture is proposed to sufficiently harvest solar energy and further to realize multipath water extraction from liquid/solid substrates. In our system, the CNT film at the air/water interface can be uniformly and alternatively transferred onto a commercial paper surface in a large scale through an interfacial capillarity transfer method with a supramolecular interaction between —OH at the surface of CNTs and paper. Due to the excellent tailorability and foldability

Dr. P. Xiao, J. He, Y. Liang, C. Zhang, J. Gu, Dr. J. Zhang, Dr. Y. Huang, Prof. T. Chen
Key Laboratory of Marine Materials and Related Technologies
Zhejiang Key Laboratory of Marine Materials and Protective Technologies
Ningbo Institute of Material Technology and Engineering
Chinese Academy of Sciences
Zhongguan West Road 1219, Ningbo 315201, China
E-mail: tao.chen@nimte.ac.cn

Dr. P. Xiao, J. He, Y. Liang, J. Gu, Dr. J. Zhang, Dr. Y. Huang, Prof. T. Chen
School of Chemical Sciences
University of Chinese Academy of Science
Beijing 100049, China

Prof. S.-W. Kuo
Department of Material and Optoelectronic Science
Center of Crystal Research
National Sun Yat-sen University
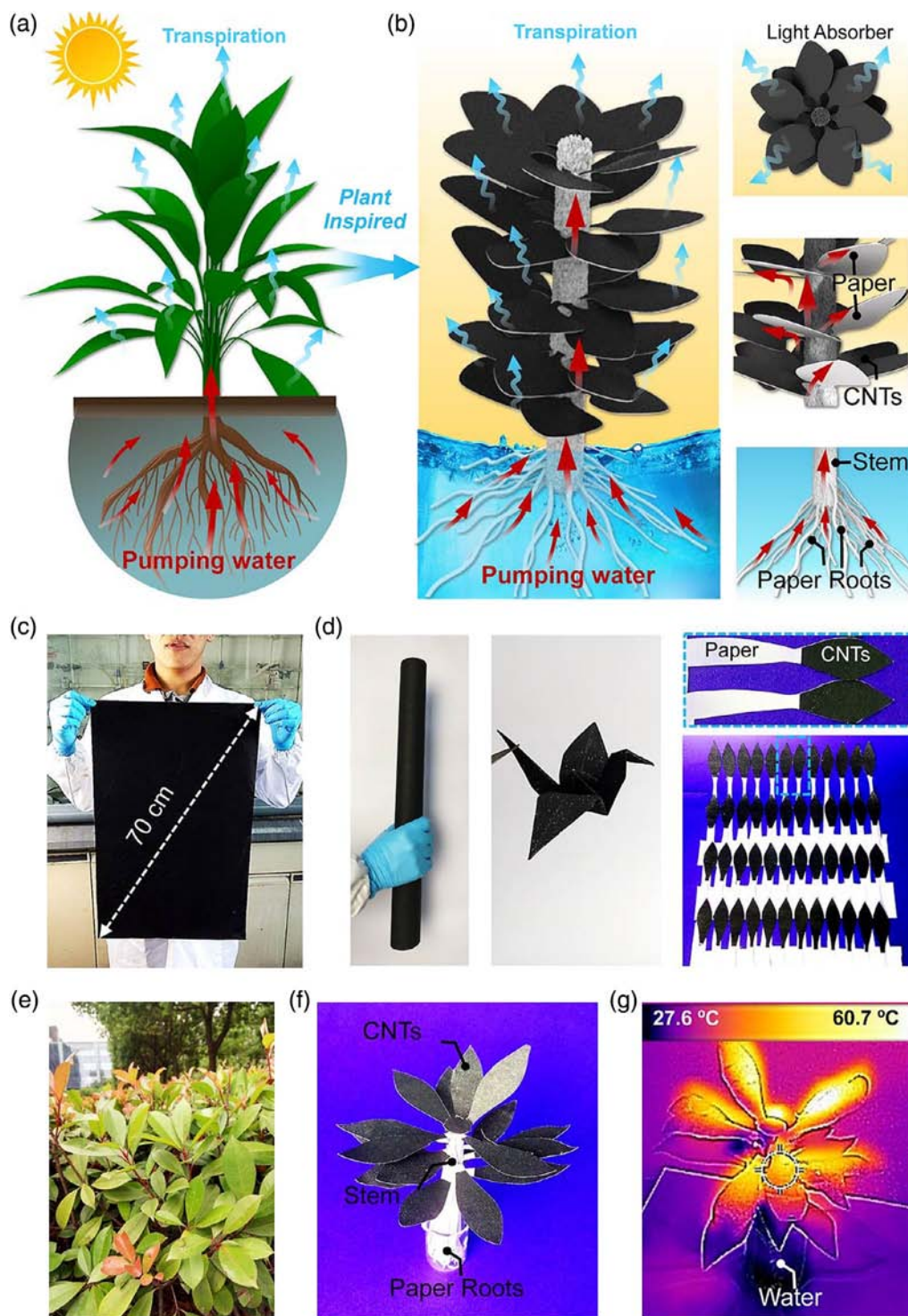Kaohsiung 804, Taiwan

Figure 1. a) Schematic of a plant pumping water from the groundwater. b) Illustration of the plant-inspired 3D hierarchical structures through the well-designed assembly of carbon-based papers via the combination of kirigami and origami. c) Photograph of the large-area CNTs/paper hybrid film fabricated at the air/water interface. d) The film presents excellent flexibility, foldability, and tailorability. e) Photograph of plants leaves grown in the 3D direction. f) The well-designed 3D HPF. g) IR image of the 3D HPF with roots immersed in water under 1 sun.

of the resulted CNTs/paper (CP) 2D Janus (endothermic CNTs/hydrophilic and adiabatic paper) hybrid, it was further cut into specific geometries and subsequently assembled to 3D plant-like

architectures. In the 3D system, paper-based roots and stems were used to perform water pumping and transportation, individually. More importantly, the leaf-like CP for light absorption was

projected to keep away from the water, which can significantly block the pathways of heat diffusion to the water subphase. Furthermore, attributed to the tridimensional framework of the 3D structure, even water from the sand ground could be effectively extracted, providing a novel pathway of 3D solar-to-thermal technology for water purification under some extreme conditions.

2. Results and Discussion

As schematically shown in Figure 1b, a 3D hierarchically plant-like generator (HPG) was exquisitely designed by selectively transferring CNT films onto papers, tailoring them into desired geometries, and assembling to hierarchical 3D structures. The as-prepared 3D HPG is composed of three components, including CP-based leaves as light absorbers, paper-based stems for water transportation/thermal insulation, and paper-based roots for water pumping. In this system, a commercial paper was selected to act as the water channel and thermal insulation layer due to its favorable intrinsic properties, wide accessibility, and low expenses. Through a capillarity-driven interfacial transfer strategy, a large-area CP was first achieved successfully (Figure 1c). The resultant CP can experience rigorous bending and folding process without remarkable breakage, demonstrating excellent stability and portability. To mimic the shape of leaves, traditional Chinese kirigami was used to realize a desired shape (Figure 1d). In plants,

the natural leaves can establish themselves to achieve a multilevel growth to increase the effective lighting area (Figure 1e). In our plant-inspired design, the tailored CPs were orderly integrated into a hierarchical 3D framework. As shown in Figure 1f, 3D HPG with well-designed leaves, stems, and roots was readily realized. As expected, when it was embedded into water, capillarity enabled water transportation can happen from the roots and stems to the leaves (Figure S1, Supporting Information). Once illuminated under 1 sun, IR radiation image presents a remarkable temperature gradient from leaves to the roots, which indicates that solar thermal conversion is strictly confined in the leaves, rather than the stems, roots, and even bulk water (Figure 1g).

For the fabrication of the self-supported CNT film, a variety of strategies were developed in our group.[38–42] In this system, due to the slight oxidation of the CNTs, it can be dispersed uniformly into the ethanol solvent in a stable state (Figure S2, Supporting Information). As shown in **Figure 2**a, a large-scale CNT film was self-assembled on the water surface through a spray-coating and capillary force driving compression strategy (Figure S3, Supporting Information),[43–46] followed by an in situ transfer onto the paper surface. Based on the capillarity transfer mechanism, when the water penetrated through the porous CNT film to the fibrous paper, the generated capillary force can effectively enhance the supramolecular interaction between —OH on the surface of the CNT film and paper (Figure S4 and S5, Supporting Information). Specifically, compared with the dense
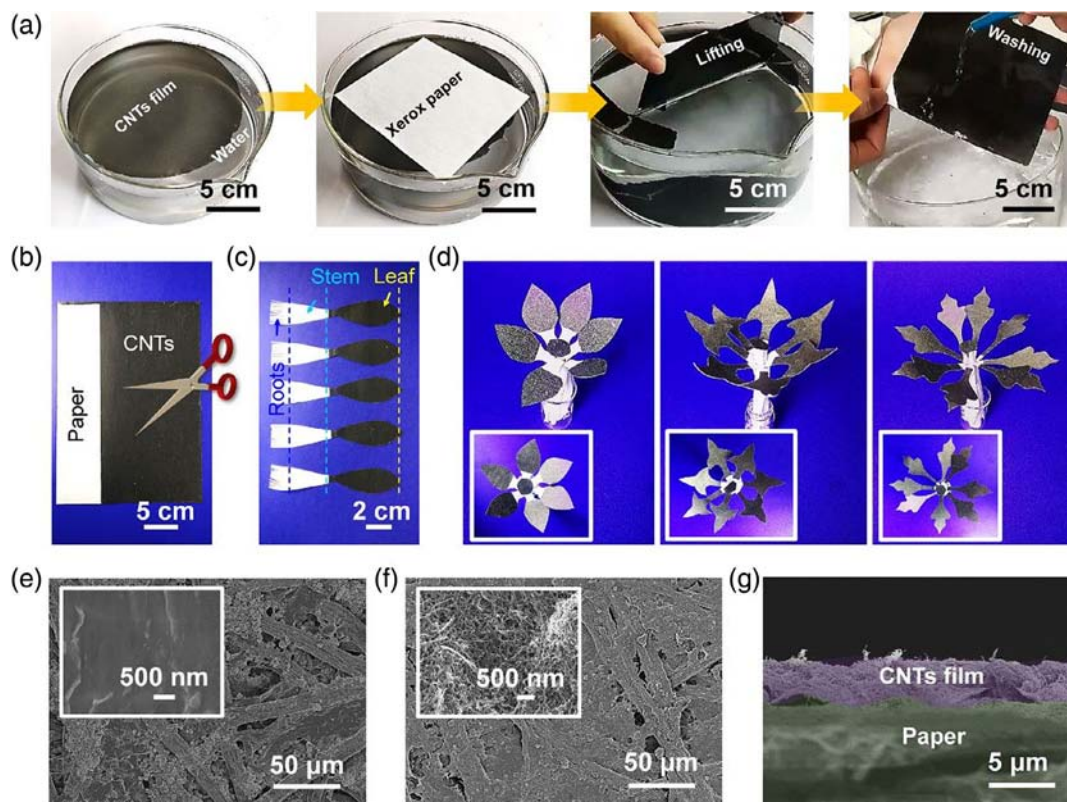

Figure 2. a) Photographs of the CNT films assembled on the water substrate were in situ transferred onto the xerox paper surface through a capillary force-driven transfer way. b) The resultant CNTs/paper film after selectively transferred and drying process. c) The film is tailored into artificial leaves with paper-based stem and roots. d) A variety of shaped leavers were easily achieved and assembled into desired 3D structures. SEM images of e) paper side and f) CNT side of the film. g) Cross-sectional image of the resultant film.

graphene sheet-based films, the self-assembled porous CNT network can significantly provide a desirable channel for the water from the paper substrates. After peeling off from the water surface, a stable CP was readily acquired and could endure rigorous washing procedure without apparent delamination. Note that this robust strategy allows a nondestructive and multiple transfer, resulting in uniform CP with a well-controlled CNT layer thickness (Figure S6, Supporting Information). Moreover, this simple and reproducible transfer manner allows us to realize large-scale production in a simple and scalable way (Figure S7, Supporting Information).

Significantly, the as-prepared CNT film can be selectively transferred onto the specific position of the paper surface with a sharp interface for constructing specific structures (Figure 2b). The resultant CP demonstrates good uniformity and flexibility, which can be further folded to a smaller size and restored to the original state with the aid of water (Figure S8, Supporting Information). Especially, it could be readily cut into certain

geometries with controllably functional zones (Figure 2c). To mimic the diversity of the plants, a variety of shaped leaves were assembled to construct 3D HPG (Figure 2d and Figure S9, Supporting Information). It is noted that leaves with specific shapes enable their own spatial arrangements for maximum light absorption. As a proof of concept, the common long elliptic leaves were selected in our system. Microscopically, the morphology and cross-sectional information of the as-prepared CP were confirmed by SEM images, which indicate a distinct morphology difference between the paper side and CNTs one (Figure 2e,f). Figure 2g and Figure S10, Supporting Information, further strongly evidenced the bilayer structure. As shown in Figure S11, Supporting Information, the porous structures of the CNT film further ensure the continuous transportation of the water from the bulk phase to the paper surface. For more structural information, Raman characterization was also measured, representing characteristic peaks of D, G, and 2D bands of CNTs (Figure S12, Supporting Information).
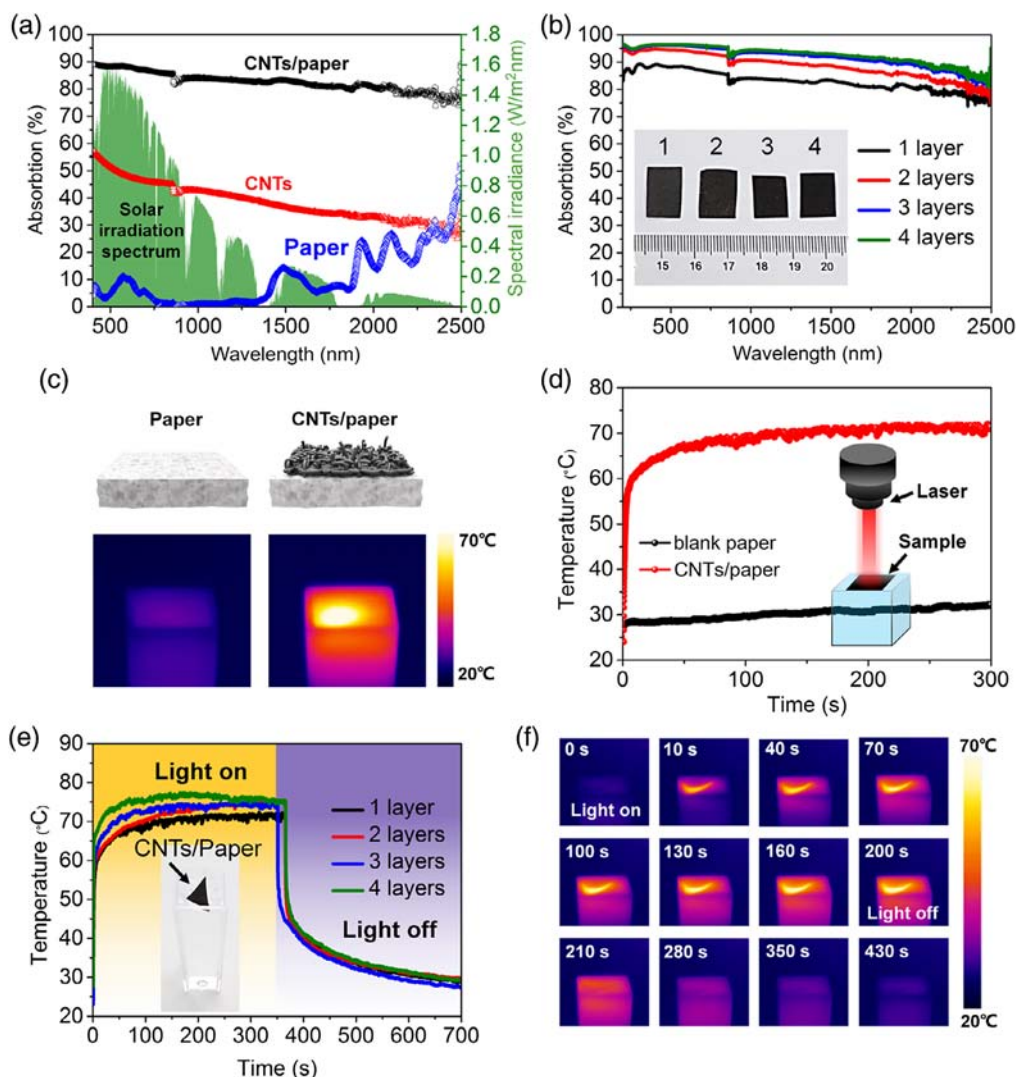

Figure 3. a) Solar spectral irradiance (AM 1.5 G) and absorption curves of paper blank, CNT film, and CNTs/paper. b) Absorption curves of CNTs/paper with different layers of CNT films. c) IR images of papers with/without CNT films under laser. d) Temperature versus time curves of paper and CNTs/paper. e) Temperature versus time curves of CNTs/paper with different CNT film layers. f) 2D IR images of four layers CNTs/paper with/without laser.

Furthermore, optical properties of the CNTs/paper were measured with an ultraviolet visible-near-infrared (UV–vis–NIR) spectrophotometer. Compared with the CNT film and paper, the achieved CP demonstrated higher absorption in all spectral ranges (**Figure 3**a). Moreover, to optimize the evaporation performance, different CNT layer thicknesses ranging from ≈0.6 μm (one layer) to ≈2.2 μm (four layers) were also investigated. With the increase of the CNT load, the absorption of the as-prepared CP presented a gradual increasing tendency. It was found that CP with four layers can absorb almost 95% of UV, 96% of visible, and 90% of IR solar irradiation with a total absorption capacity of 93.7% over the whole solar spectrum (Figure 3b). Due to the excellent parallel light and stable power density, the laser beam (a wavelength of 808 nm with a power density of 3 W and a spot size of 0.9 cm in diameter) was selected to explore the solar thermal conversion performance of the CP. Figure 3c shows the IR images of the blank paper and CP floated on the water surface

taken at different times. The CP exhibits a sharp color change with an equilibrium temperature of ≈70 °C within 300 s, whereas the blank paper presents no obvious temperature change with ≈32 °C (Figure 3d). The result strongly evidences that the CNT layers can significantly enhance the efficiency of solar thermal conversion. With the increase in the CNT layer, the equilibrium temperature of CP rises gradually, ranging from ≈70 to ≈75 °C, which corresponds well with the improved optical properties of increased CNT layers (Figure 3e and Figure S13, Supporting Information). From the IR image in Figure 3f, it can be found that the solar-to-thermal conversion was strictly confined in the triangular-shaped CP surface.

To further investigate the solar vaporization performance of the CP, a series of water evaporation experiments were conducted under simulated solar illumination (**Figure 4**a). The bilayer structures of CP can significantly decrease the heat diffusion from the solar absorbers to the water subphase, which can effectively
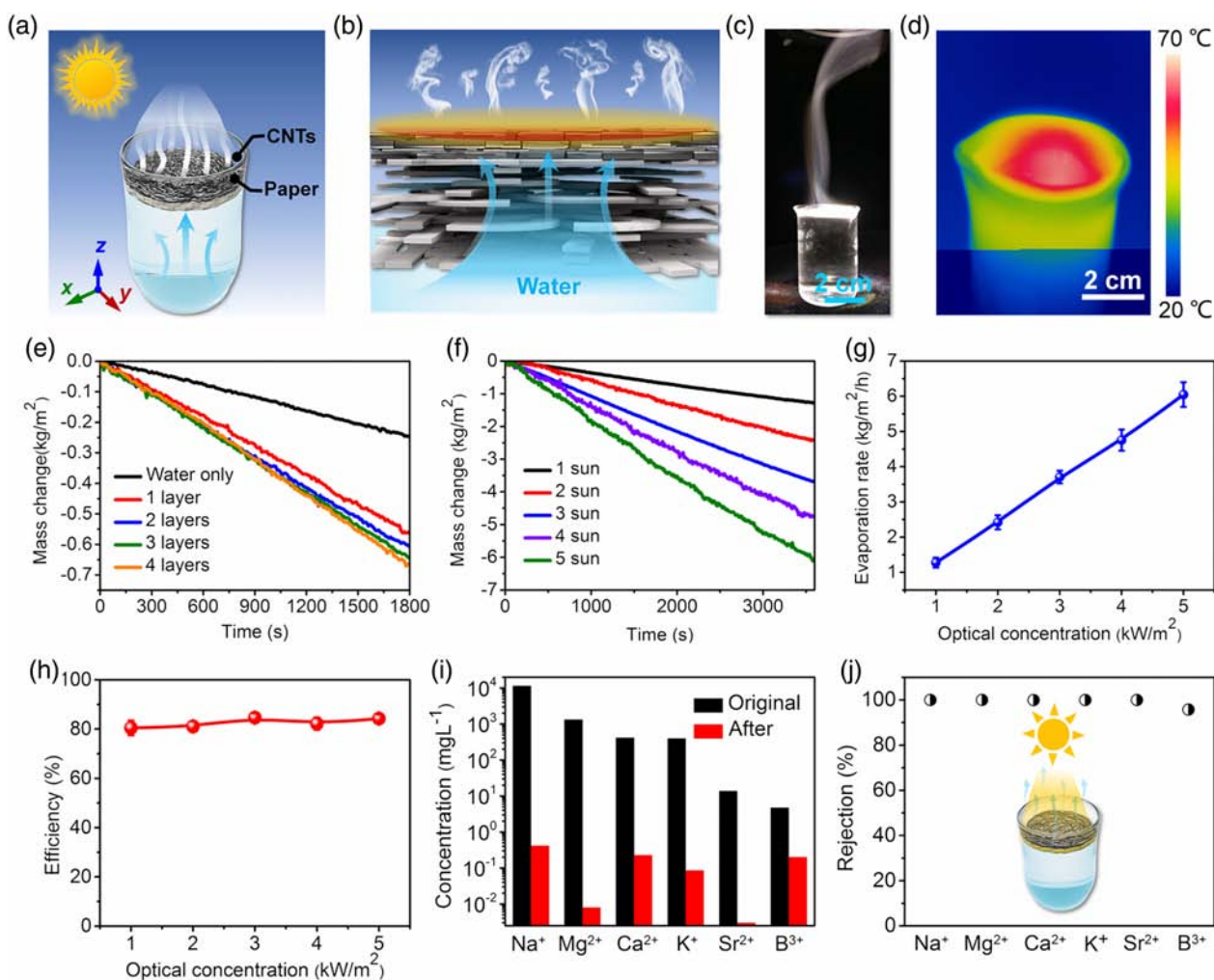

Figure 4. a) Sketch of the water evaporation of the CNTs/paper film at the air/water interface under solar irradiation. b) The evaporation mechanism of the bilayer structure. c) Photograph of abundant steam generated under solar irradiation of 5 kW m^{-2}. d) IR image of the CNTs/paper floated on the water surface. e) Mass change versus time curves of water and films with different CNT layers under 1 sun irradiation (1 kW m^{-2}). f) Mass change over time curves of film with four-layer CNTs under different sun irradiation. g) The corresponding evaporation rate in (f) under different optical concentration. h) Solar steam efficiencies under various sun irradiation. i) The measured ion concentration of six simulated seawater samples before and after desalination. j) The ion rejection of simulated seawater sample.

enhance the solar-to-thermal conversion (Figure 4b).[6,8,22,47] Under a simulated solar beam with 5 sun (5 kW m^{-2}), the steam can be clearly observed with naked eyes, enabling a continuous and stable water evaporation even under a high solar intensity (Figure 4c). Furthermore, the IR image was used to monitor the temperature distribution of the bilayer CP floated at the air/water interface. Upon illumination, the temperature on the CP surface can rapidly increase up to ≈75 °C within 2 min (Figure 4d). In addition, the weight changes of CP with a series of CNT thickness over time under 1 sun are also shown in Figure 4e. Superior to blank water, the CP demonstrates a higher weight loss. To optimize the evaporation efficiency, the thickness of the solar absorption layer was also evaluated, which represents a positive correlation with the evaporation rate. Nevertheless, when further increasing the CNT layers (such as paper hybrid with a five-layer CNT film), the CP exhibits smaller capillary pores of the CNT network, which may severely block the pathway of the water transportation, resulting in decreased water evaporation rate (Figure S14, Supporting Information). Note that light absorption and water transportation are both important factors that can affect the performance of the CP. Due to the competitive

evaporation rate of the four-layer CP, it was preferably chosen in further experiments.

To investigate the capability of solar vaporization under different sunlight, the mass change curves under solar intensity from 1 to 5 sun are shown in Figure 4f. The result shows that the calculated evaporation rate is found to increase linearly with the optical concentration, ensuring a continuous and robust evaporation platform (Figure 4g). The evaporation efficiency that is defined as $\eta = mh/I_{sun}$ can also be calculated, in which m denotes the mass flux, h is the total enthalpy of the liquid–liquid sensible heat from the initial temperature to the final temperature and liquid–vapor latent heat, and I_{sun} is the total power of solar illumination.[17,48] Through the adjustment of optical concentration, the efficiencies show prominent enhancement ranging from 80% to 84% (Figure 4h). As a potential material for water distillation, the CP with four layers was used to generate clean water under 1 sun using a homemade device. As shown in Figure 4i, the concentrations of six ions of Na$^+$, Mg^{2+}, Ca^{2+}, K$^+$, Sr^{2+}, and B^{3+} are effectively reduced with an average ion rejection of 99.27% (Figure 4j). Especially, according to the World Health Organization (WHO) standard, the calculated
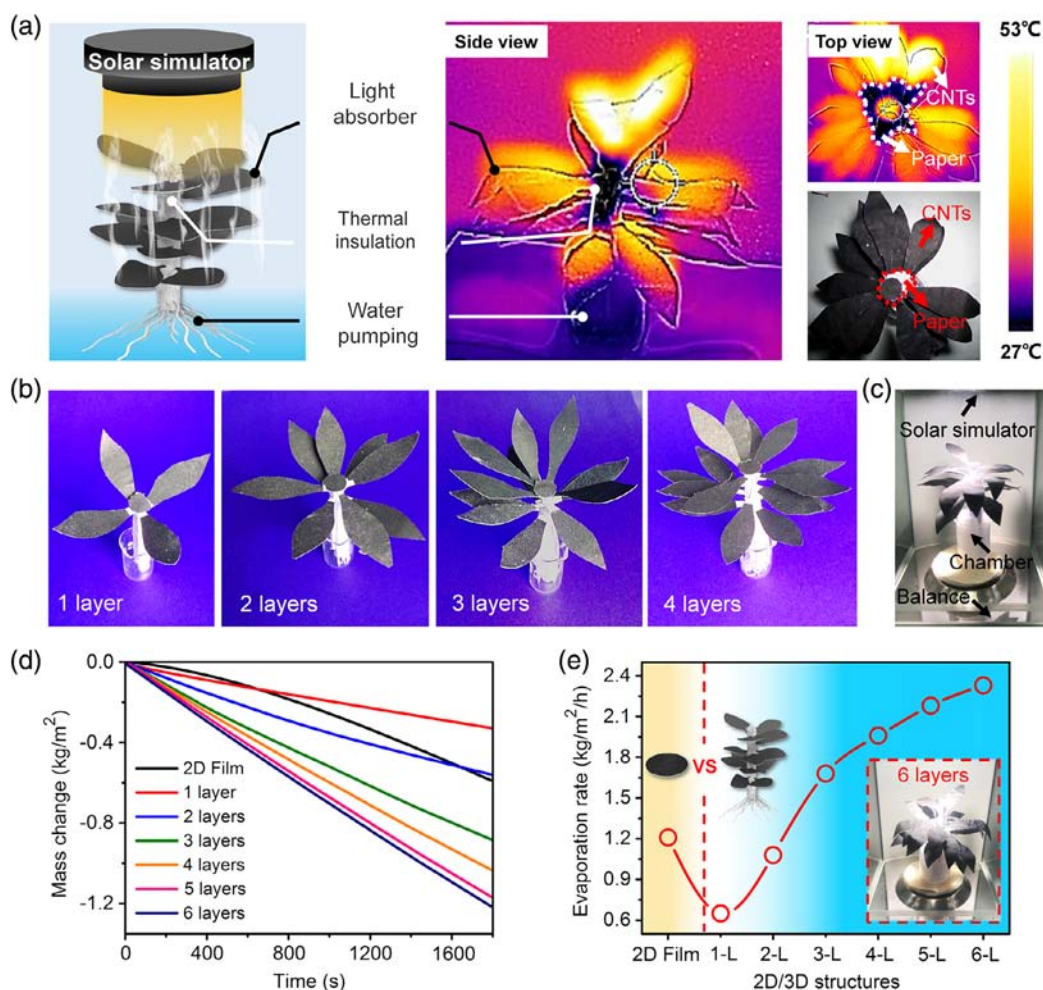

Figure 5. a) The mechanism of high-efficient evaporation of the 3D HPG and corresponding IR images under 1 sun. b) Photographs of 3D HPG decorated with different layers of leaves to achieve a well-controlled evaporation. c) The evaporation apparatus. d) Mass change versus time curves of the 2D film and various 3D HPG. e) Mass change curve of different light absorbers structures.

ADVANCED
SCIENCE NEWS
www.advancedsciencenews.com

Solar
RRL
www.solar-rrl.com

concentration of Na$^+$ ions is below the salinity levels, indicating a significant potential for purified water collection.

As the 2D film demonstrates an effective water distillation performance, it could be further integrated into a biomimetic 3D architecture via a hierarchical assembly. A typical 3D HPG includes light absorbers, water transportation/thermal insulators, and water pumping (**Figure 5**a). Compared with the 2D structure, the multi-assembled 3D one was provided with more effective lighting area under the same projected area. It is noted that the applied intensity of the simulated sunlight on 3D HPG is determined using the bottom layer of the 3D structure as the measuring baseline in the laboratory experiments. From the IR image in Figure 5a, it can be observed that the solar-to-thermal conversion is strictly confined in the light absorbers part. Notably, to achieve a favorable water transportation, the CPs used in the 2D and 3D systems were both treated with oxygen plasma for favorable hydrophilic properties (Figure S15 and S16, Supporting Information). In our 3D system, there are four leaves in one layer. Typically, the performance of the 3D HPG could

be further adjusted by increasing the layers of the leaves (Figure 5b,c). Due to the lower effective area of light absorption with one and two layers, the water evaporation rates are lower than that of the 2D film (Figure 5d). When more layers ($\geq$3 layers) are introduced into the 3D HPG, the values experience a remarkable increase process, which are higher than that of the 2D film. Note that attributed to the spatial shielding effect of the multilayered leaves, the increasing tendency of the effective area slowed down, which could be clearly observed in the evaporation rates of five and six layers of 3D HPG (Figure 5e). As a result, the final evaporation rate can rise up to $2.38\,\mathrm{kg\,m^{-2}\,h^{-1}}$ with six-layer 3D HPG, representing powerful potential in high-efficient solar distillation (Figure 5e).

To investigate the solar desalination capability of the 3D HPG, a well-designed prototype was fabricated and used to conduct solar steam generation experiments in **Figure 6**a. In the controlled experiments, the 2D film and 3D HPG with the same projected area were used to calculate the final water evaporation rate (Figure 6b). In a sealed chamber, the vapor was generated
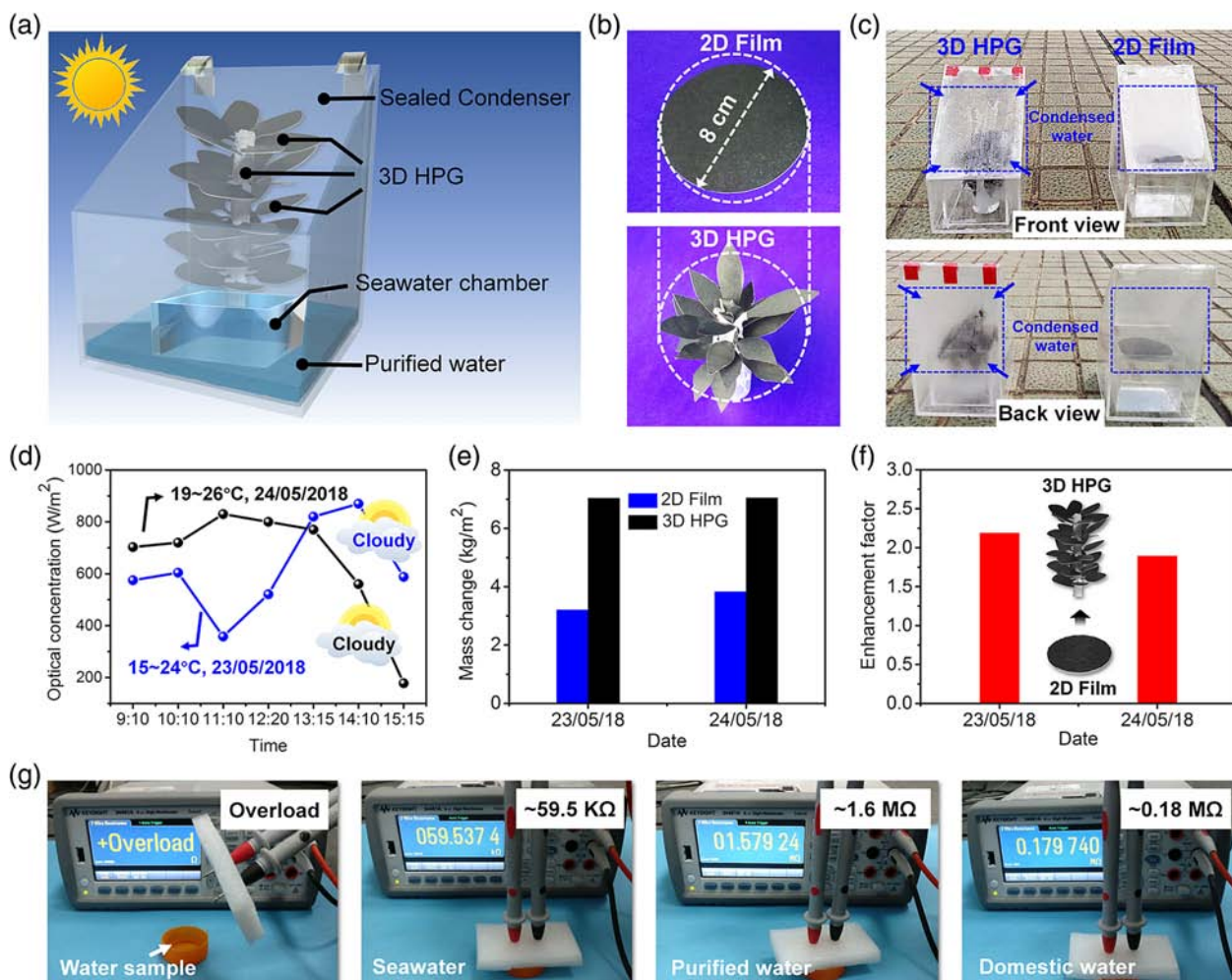

Figure 6. a) Sketch of the designed distilled water collection apparatus. b) Photographs of the 2D film and 3D HPG with the same projected area. c) Photographs of water distillation experiment under the natural light in sealed chambers. d) Optical concentration versus time curves of different days at certain temperature and humidity. e) Average evaporation rates of the 2 days. f) The enhancement factor for 3D HPG versus the 2D film. g) Evaluation of water purity with a constant electrode distance.

from the light absorbers surface under solar irradiation and subsequently condensed into liquid when it arrived at the relatively cold condensation roof. Compared with the 2D film, more water gathered on the roof surface and flowed in streams in the 3D HPG system (Figure 6c). To explore the practical performance of distillation, two consecutive days that were partly sunny days
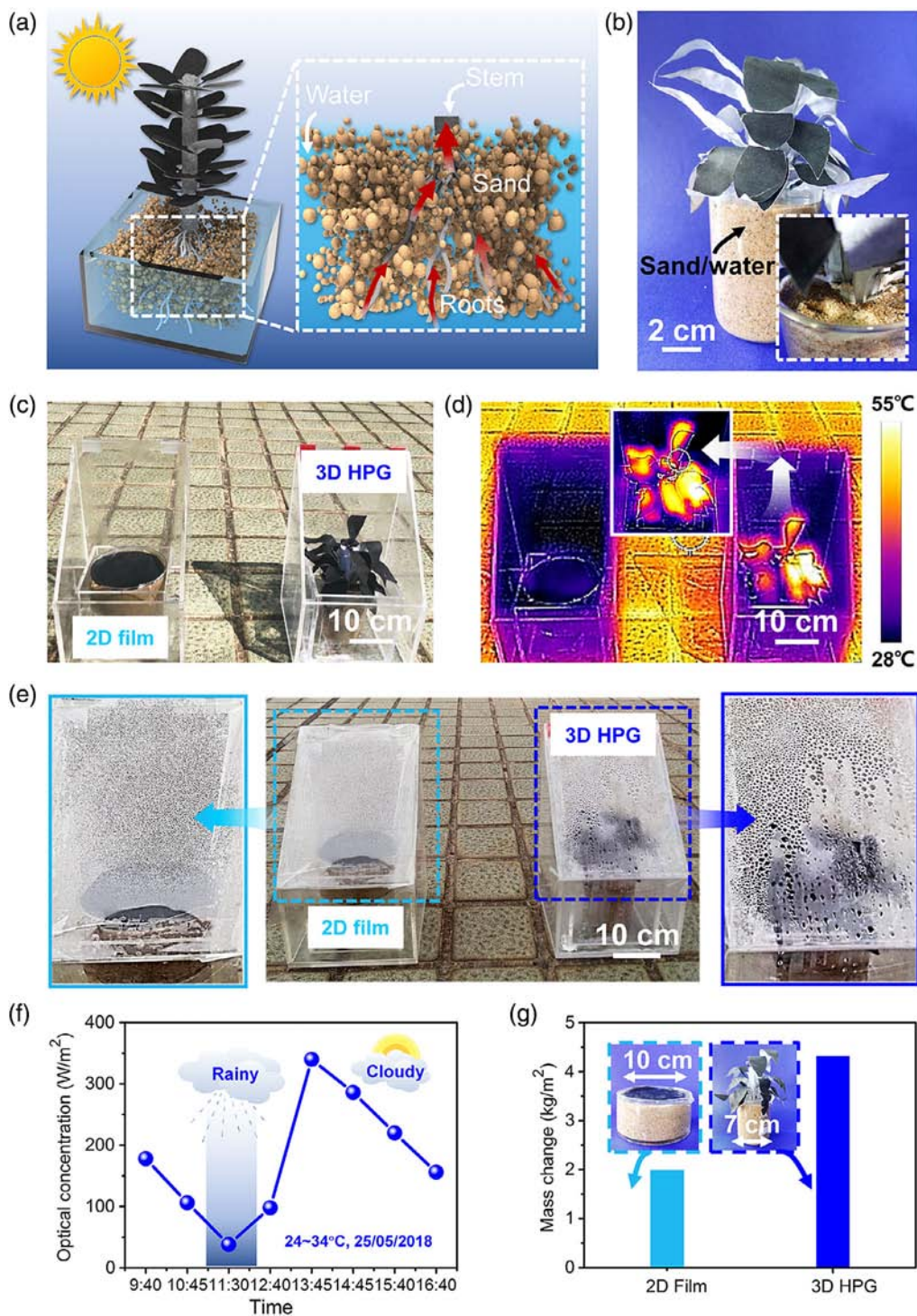

Figure 7. a) Schematic of the artificial plants embedded into the sandy water. b) Photograph of the artificial plant rooted in the sandy water. Inset: the amplified photograph of 3D HPG rooted in the sand. c) Photographs of the 2D film and 3D HPG in chambers under natural sunlight. d) The IR image of the 2D film and 3D HPG. Inset: the amplified IR image of the 3D HPG. e) Photograph of the 2D and 3D generators in sealed chambers after 2 h. f) Optical concentration versus time curve at a certain day. g) Mass change histogram of the 2D film and 3D HPG, demonstrating a remarkable increase of the water evaporation.

with roaming cloud (May 23 and 24, 2018) were selected to collect distilled water. Attributed to the cloudy factor, the optical concentration varied dramatically (Figure 6d). After distillation, the average mass changes for the 2D film and 3D HPG were both measured, enabling $3.21/7.04 \, \text{kg m}^{-2}$ on May 23 and $3.83/7.05 \, \text{kg m}^{-2}$ on May 24 of purified water during the 6 h outdoor irradiation, exhibiting significant potentials for efficient purified water supply (Figure 6e). Note that the mass changes in the outdoor experiments were all calculated through the collected purified water from the chambers (Figure S17, Supporting Information). To precisely illustrate this efficiency improvement, an enhancement factor that is denoted as the evaporation rate ratio of the 3D HPG and 2D film is calculated, demonstrating a prominent promotion of 2.19 and 1.90 for 2 days (Figure 6f). Furthermore, resistance test with a multimeter at a constant distance between two electrodes was also conducted by measuring the ohmic value of different samples. As shown in Figure 6g, the simulated seawater, purified water, and domestic water presented the resistance values of 0.06, 1.6, and $0.18 \, \text{M}\Omega$, respectively, exhibiting an excellent seawater distillation.

More importantly, when the 3D HPG was implanted into the sand ground, the ground water could be continuously extracted from the paper roots to the CP-based leave surfaces due to the strong capillary force generated from the fibrous structures (**Figure 7**a).[31] As the specific bionic structure of the 3D HPG can be deeply embedded into the sand/water mixture, it can stand steadily with all the leaves exposed to the air for maximum light absorption (Figure 7b). As shown in Figure 7c, the 2D film and 3D HPG were both placed on the sandy water surface for further water evaporation tests. The IR image in Figure 7d clearly presents that the achieved temperature of 3D HPG is higher than that of the 2D film attributed to decreased heat diffusion from the specific 3D structure to the bulk water. Furthermore, the self-supported 3D HPG can prominently decrease the heat diffusion to the sandy water. In comparison with the 2D film, more and larger water droplets were condensed on the chamber roof surface and flowed down in the 3D HPG system after 1 h natural light illumination (Figure 7e and Figure S18, Supporting Information). The outdoor experiment was conducted from 09:40 to 16:40 under natural sunlight with an average solar heat flux of $\approx 0.18 \, \text{kw m}^{-2}$ (Figure 7f). In a sealed chamber, the purified water could be effectively collected, in which the 2D film and 3D HPG represent 0.28 and $0.62 \, \text{kg m}^{-2} \text{h}^{-1}$, respectively (Figure 7g). The superior adaptive capability of the 3D HPG can tremendously extend the scope of applications under extreme environment.

3. Conclusions

In conclusion, enlightened by the natural plants with an adaptable capability, we propose a cost-effective, scalable, and novel approach to construct a well-designed artificial tree with editable structures toward multipath water extraction. Through a robust interfacial carbon nanotubes self-assembly and in situ capillarity driving transfer strategy, a bilayer CNTs/paper 2D Janus (endothermic CNTs/hydrophilic and adiabatic paper) hybrid membrane in a large scale can be readily achieved. The resultant bilayer hybrid as building blocks could be further tailored into desired geometries and multi-assembled into a 3D artificial tree for an enhanced and controllable 2D/3D solar vaporization. Significantly, it can even extract purified water from the sand ground, demonstrating significant potentials in water distillation under some complex environments.

4. Experimental Section

Materials: The raw carbon nanotubes (CNTs) (length, about 10–30 μm; diameter, about 10–30 nm; —COOH %, about 1.5 wt%) with a purity of over 90% were acquired from Chengdu Organic Chemistry Co., Ltd. and were rinsed thoroughly with anhydrous ethanol and dried in a stream of nitrogen before use. General chemicals in chemical reagent grade were used as received from Sinopharm Chemical Reagent.

Formation of CNTs Film: The CNT powders were first dispersed in an anhydrous ethanol solution, followed by strong ultrasonication for at least 5 h to form a stable dispersion with appropriate aging time. The as-prepared suspensions spread onto the water surface by the spray-coating method for appropriate volume, resulting in uniform Langmuir monolayers formed at the liquid/air interface. Subsequently, a porous sponge was used to put on one side of the interface to quickly siphon water from the system. Notably, the homogenous Langmuir monolayers were closely packed toward the opposite direction of the syphone direction. When the CNTs film cannot be further compressed by the sponge, the resultant film is ultimately formed, indicating a closely packed structure.

Fabrication of CNTs/Paper: A commercial xerox paper was gently put onto the surface of the as-prepared CNT film at the air/water interface. With strong capillarity of the fibrous structures of the paper, water from the subphase can be absorbed into the paper through the porous structures of the CNT film. As a result, the CNT film could be tightly attached onto the surface of the paper through the capillary force. When the paper was completely wetted, it could spread smoothly on the water surface, indicating a successful transfer of the CNT film. The resultant CNTs/paper can be directly peeled from the water surface, followed by a rigorous rinsing procedure using deionized water.

Solar Vaporization Experiments: Square CNTs/paper samples (9 mm in diameter) with different CNT film thicknesses were floated on the water surface in a plastic tube, which were irradiated by a solar simulator (HM-Xe500W) equipped with the optical filter for AM 1.5G spectrum. The mass changes were measured by an electronic balance with an accuracy of 0.0001 g at constant temperature and humidity.

Characterization: Field-emission scanning electron microscopy (FESEM) images were obtained with an FE scanning electron microanalyzer (Hitachi-S4800, 4 kV). Transmission electron microscopy (TEM) was recorded using a transmission electron microscope (JEM-2100F, accelerating voltage of 200 kV). TEM samples were prepared by dropping a diluted aqueous solution of CNTs onto carbon-coated copper grids and dried in air. Raman measurements were performed at room temperature on a Raman system (inVia-reflex, Renishaw) with confocal microscopy. The solid-state diode laser (532 nm) was used as an excitation source with a frequency range of $3000-1000 \, \text{cm}^{-1}$. Optical transmittance of the films was probed using UV–vis–NIR spectra, which were obtained with a Lambda 950 spectrophotometer from PerkinElmer Instrument Co., Ltd., USA. Static water contact angles were measured at room temperature using the sessile drop method and image analysis of the drop profile using the instrument (OCA-20, Dataphysics) with a charge-coupled device camera and an image analysis processor. An IR camera (Optris PI400) with a resolution of 382×288 pixels was used to realize a real-time recording of the surface temperature of the CNT film. The data were analyzed by the PI connect software.

Supporting Information

Supporting Information is available from the Wiley Online Library or from the author.

Acknowledgements

Conflict of Interest

The authors declare no conflict of interest.

Keywords

[1] M. A. Shannon, P. W. Bohn, M. Elimelech, J. G. Georgiadis, B. J. Marinas, A. M. Mayes, *Nature* **2008**, *452*, 301.

[2] L. A. Weinstein, J. Loomis, B. Bhatia, D. M. Bierman, E. N. Wang, G. Chen, *Chem. Rev.* **2015**, *115*, 12797.

[3] C. Li, Y. Goswami, E. Stefanakos, *Renewable Sustainable Energy Rev.* **2013**, *19*, 136.

[4] G. Ni, G. Li, S. V. Boriskina, H. Li, W. Yang, T. Zhang, G. Chen, *Nat. Energy* **2016**, *1*, 16126.

[5] M. Elimelech, W. A. Phillip, *Science* **2011**, *333*, 712.

[6] Y. Liu, S. Yu, R. Feng, A. Bernard, Y. Liu, Y. Zhang, H. Duan, W. Shang, P. Tao, C. Song, T. Deng, *Adv. Mater.* **2015**, *27*, 2768.

[7] L. Zhou, Y. Tan, J. Wang, W. Xu, Y. Yuan, W. Cai, S. Zhu, J. Zhu, *Nat. Photonics* **2016**, *10*, 393.

[8] F. J. Chen, A. S. Gong, M. W. Zhu, G. Chen, S. D. Lacey, F. Jiang, Y. F. Li, Y. B. Wang, J. Q. Dai, Y. G. Yao, J. W. Song, B. Y. Liu, K. Fu, S. Das, L. B. Hu, *ACS Nano* **2017**, *11*, 4275.

[9] K. Bae, G. Kang, S. K. Cho, W. Park, K. Kim, W. J. Padilla, *Nat. Commun.* **2015**, *6*, 10103.

[10] J. Wang, Y. Li, L. Deng, N. Wei, Y. Weng, S. Dong, D. Qi, J. Qiu, X. Chen, T. Wu, *Adv. Mater.* **2017**, *29*, 1603730.

[11] S. V. Boriskina, H. Ghasemi, G. Chen, *Mater. Today* **2013**, *16*, 375.

[12] L. Zhang, B. Tang, J. Wu, R. Li, P. Wang, *Adv. Mater.* **2015**, *27*, 4889.

[13] Q. S. Jiang, H. G. Derami, D. Ghim, S. S. Cao, Y. S. Jun, S. Singamaneni, *J. Mater. Chem. A* **2017**, *5*, 18397.

[14] Q. M. Chen, Z. Q. Pei, Y. S. Xu, Z. Li, Y. Yang, Y. Wei, Y. Ji, *Chem. Sci.* **2018**, *9*, 623.

[15] H. Ghasemi, G. Ni, A. M. Marconnet, J. Loomis, S. Yerci, N. Miljkovic, G. Chen, *Nat. Commun.* **2014**, *5*, 4449.

[16] J. L. Yang, Y. S. Pang, W. X. Huang, S. K. Shaw, J. Schiffbauer, M. A. Pillers, X. Mu, S. R. Luo, T. Zhang, Y. J. Huang, G. X. Li, S. Ptasinska, M. Lieberman, T. F. Luo, *ACS Nano* **2017**, *11*, 5510.

[17] P. P. Zhang, J. Li, L. X. Lv, Y. Zhao, L. T. Qu, *ACS Nano* **2017**, *11*, 5087.

[18] Y. Yang, R. Q. Zhao, T. F. Zhang, K. Zhao, P. S. Xiao, Y. F. Ma, P. M. Ajayan, G. Q. Shi, Y. S. Chen, *ACS Nano* **2018**, *12*, 829.

[19] H. Y. Ren, M. Tang, B. L. Guan, K. X. Wang, J. W. Yang, F. F. Wang, M. Z. Wang, J. Y. Shan, Z. L. Chen, D. Wei, H. L. Peng, Z. F. Liu, *Adv. Mater.* **2017**, *29*, 1702590.

[20] Y. J. Li, T. T. Gao, Z. Yang, C. J. Chen, W. Luo, J. W. Song, E. Hitz, C. Jia, Y. B. Zhou, B. Y. Liu, B. Yang, L. B. Hu, *Adv. Mater.* **2017**, *29*, 1700981.

[21] X. Z. Hu, W. C. Xu, L. Zhou, Y. L. Tan, Y. Wang, S. N. Zhu, J. Zhu, *Adv. Mater.* **2017**, *29*, 1604031.

[22] Q. Jiang, L. Tian, K.-K. Liu, S. Tadepalli, R. Raliya, P. Biswas, R. R. Naik, S. Singamaneni, *Adv. Mater.* **2016**, *28*, 9400.

[23] Y. Ito, Y. Tanabe, J. Han, T. Fujita, K. Tanigaki, M. Chen, *Adv. Mater.* **2015**, *27*, 4302.

[24] P. Yang, K. Liu, Q. Chen, J. Li, J. Duan, G. Xue, Z. Xu, W. Xie, J. Zhou, *Energy Environ. Sci.* **2017**, *10*, 1923.

[25] Z. Yin, H. Wang, M. Jian, Y. Li, K. Xia, M. Zhang, C. Wang, Q. Wang, M. Ma, Q.-S. Zheng, Y. Zhang, *ACS Appl. Mater. Interfaces* **2017**, *9*, 28596.

[26] Y. B. Yang, X. D. Yang, L. N. Fu, M. C. Zou, A. Y. Cao, Y. P. Du, Q. Yuan, C. H. Yan, *ACS Energy Lett.* **2018**, *3*, 1165.

[27] X. Yang, Y. Yang, L. Fu, M. Zou, Z. Li, A. Cao, Q. Yuan, *Adv. Funct. Mater.* **2018**, *28*, 1704505.

[28] R. Y. Li, L. B. Zhang, L. Shi, P. Wang, *ACS Nano* **2017**, *11*, 3752.

[29] H. Lin, X. Wang, L. Yu, Y. Chen, J. Shi, *Nano Lett.* **2017**, *17*, 384.

[30] C. J. Chen, Y. J. Li, J. W. Song, Z. Yang, Y. Kuang, E. Hitz, C. Jia, A. Gong, F. Jiang, J. Y. Zhu, B. Yang, J. Xie, L. B. Hu, *Adv. Mater.* **2017**, *29*, 1701756.

[31] M. W. Zhu, Y. J. Li, G. Chen, F. Jiang, Z. Yang, X. G. Luo, Y. B. Wang, S. D. Lacey, J. Q. Dai, C. W. Wang, C. Jia, J. Y. Wan, Y. G. Yao, A. Gong, B. Yang, Z. F. Yu, S. Das, L. B. Hu, *Adv. Mater.* **2017**, *29*, 1704107.

[32] N. Xu, X. Z. Hu, W. C. Xu, X. Q. Li, L. Zhou, S. N. Zhu, J. Zhu, *Adv. Mater.* **2017**, *29*, 1606762.

[33] S. D. Zhuang, L. Zhou, W. C. Xu, N. Xu, X. Z. Hu, X. Q. Li, G. X. Lv, Q. H. Zheng, S. N. Zhu, Z. L. Wang, J. Zhu, *Adv. Sci.* **2018**, *5*, 1700497.

[34] F. Zhao, X. Zhou, Y. Shi, X. Qian, M. Alexander, X. Zhao, S. Mendez, R. Yang, L. Qu, G. Yu, *Nat. Nanotechnol.* **2018**, *13*, 489.

[35] X. Zhou, F. Zhao, Y. Guo, Y. Zhang, G. Yu, *Energy Environ. Sci.* **2018**, *11*, 1985.

[36] G. Ni, S. H. Zandavi, S. M. Javid, S. V. Boriskina, T. A. Cooper, G. Chen, *Energy Environ. Sci.* **2018**, *11*, 1510.

[37] P. G. Gensel, H. N. Andrews, *Am. Sci.* **1987**, *75*, 478.

[38] J. Gu, P. Xiao, J. Chen, F. Liu, Y. Huang, G. Li, J. Zhang, T. Chen, *J. Mater. Chem. A* **2014**, *2*, 15268.

[39] J. C. Gu, P. Xiao, J. Chen, J. W. Zhang, Y. J. Huang, T. Chen, *ACS Appl. Mater. Interfaces* **2014**, *6*, 16204.

[40] J. Gu, P. Xiao, Y. Huang, J. Zhang, T. Chen, *J. Mater. Chem. A* **2015**, *3*, 4124.

[41] L. Zhang, J. C. Gu, L. P. Song, L. Chen, Y. J. Huang, J. W. Zhang, T. Chen, *J. Mater. Chem. A* **2016**, *4*, 10810.

[42] L. Zhang, X. H. Zha, G. Zhang, J. C. Gu, W. Zhang, Y. J. Huang, J. W. Zhang, T. Chen, *J. Mater. Chem. A* **2018**, *6*, 10217.

[43] P. Xiao, J. Gu, C. Wan, S. Wang, J. He, J. Zhang, Y. Huang, S.-W. Kuo, T. Chen, *Chem. Mater.* **2016**, *28*, 7125.

[44] Y. Liang, P. Xiao, S. Wang, J. Shi, J. He, J. Zhang, Y. Huang, T. Chen, *J. Mater. Chem. C* **2018**, *6*, 6666.

[45] S. Wang, P. Xiao, Y. Liang, J. Zhang, Y. Huang, S. Wu, S.-W. Kuo, T. Chen, *J. Mater. Chem. C* **2018**, *6*, 5140.

[46] P. Xiao, J. Gu, J. He, S. Wang, J. Zhang, Y. Huang, S.-W. Kuo, T. Chen, *J. Mater. Chem. C* **2016**, *4*, 9750.

[47] Z. Z. Wang, Q. X. Ye, X. B. Liang, J. L. Xu, C. Chang, C. Y. Song, W. Shang, J. B. Wu, P. Tao, T. Deng, *J. Mater. Chem. A* **2017**, *5*, 16359.

[48] M. Gao, L. Zhu, C. K. Peh, G. W. Ho, *Energy Environ. Sci.* **2019**, *12*, 841.